# Magnetism-induced massive Dirac spectra and topological defects in the surface state of Cr-doped $Bi_2Se_3$-bilayer topological insulators

**C.-C. Chen[1,2], M. L. Teague[1,2], L. He[3], X. Kou[3], M. Lang[3], W. Fan[1], N. Woodward[1], K.-L. Wang[3] and N.-C. Yeh[1,2,4*]**

[1] Department of Physics, California Institute of Technology, Pasadena, CA 91125, USA
[2] Institute of Quantum Matter and Information, California Institute of Technology, Pasadena, CA 91125, USA
[3] Department of Electrical Engineering, University of California, Los Angeles, CA 90095, USA
[4] Kavli Nanoscience Institute, California Institute of Technology, Pasadena, CA 91125, USA
[*] E-mail: ncyeh@caltech.edu

**Abstract.** Proximity-induced magnetic effects on the surface Dirac spectra of topological insulators are investigated by scanning tunneling spectroscopic (STS) studies of bilayer structures consisting of undoped $Bi_2Se_3$ thin films on top of Cr-doped $Bi_2Se_3$ layers. For the thickness of the top $Bi_2Se_3$ layer equal to or smaller than 3 quintuple layers (QL), a spatially inhomogeneous surface spectral gap $\Delta$ opens up below a characteristic temperature $T_C^{2D}$. The mean value and spatial homogeneity of the gap $\Delta$ increase with decreasing temperature ($T$), increasing $c$-axis magnetic field ($H$) and increasing Cr doping level ($x$), suggesting that the physical origin of this surface gap is associated with proximity-induced $c$-axis ferromagnetism. Additionally, spatially localized resonant spectra are found near isolated Cr impurities along the boundaries of gapped and gapless regions. These spectral resonances are long-lived at $H = 0$, with their occurrences being most prominent near $T_C^{2D}$ and becoming suppressed under strong $c$-axis magnetic fields. We attribute these phenomena to magnetic impurity-induced topological defects in the spin texture of surface Dirac fermions, and discuss the feasibility of applying such "topological bits" to quantum information technology.

## 1. Introduction

The research of topological matter is an exciting frontier where the classification of quantum states of matter beyond the principle of symmetry breaking has stimulated many conceptual advances and experimental discoveries [1-3]. Among various topological matter, topological insulators (TIs) [4-8] are bulk insulators in two or three dimensions with strong spin-orbit coupling and gapless surface states protected by the time-reversal invariance (TRI). The gapless surface state of TIs consists of an odd number of Dirac cones where the energy-momentum dispersion relation is linear, similar to the massless Dirac fermions in graphene except for the odd number of Dirac cones and an additional spin-momentum locking in the former. Gapping the Dirac cones of TIs by introducing superconductivity [9-11] or magnetism [8, 9, 12, 13] via either doping or proximity effects can provide feasible means to realize the elusive Majorana modes [9, 10, 14] and topological magnetoelectric (TME) effect [12, 13] in condensed matter systems.

The underlying physics for a magnetism-induced surface gap in three-dimensional (3D) TIs is based on the assumption that the long-range ferromagnetism has a net magnetization $M$ perpendicular to the surface of the 3D-TI, and that the in-plane component of the Hamiltonian $\mathcal{H}_0$ for the surface Dirac fermions remains intact after the introduction of c-axis magnetization. Hence, the total Hamiltonian $\mathcal{H}_{\text{total}}$ for the Dirac fermions becomes

$$\mathcal{H}_{\text{total}} = \mathcal{H}_0 + \frac{1}{2} J_{\text{ex}} M \sigma_z \equiv \hbar v_F \left( k_x \sigma_y - k_y \sigma_x \right) + \frac{1}{2} J_{\text{ex}} M \sigma_z \ , \qquad (1)$$

where $\sigma_{x,y,z}$ are the Pauli matrices, $k_{x,y}$ refer to the in-plane momentum of the Dirac fermions, $J_{ex}$ denotes the ferromagnetic exchange coupling constant in the surface state, and $v_F$ is the Fermi velocity. The energy dispersion relation $E_k^{\pm}$ for the magnetism-induced massive Dirac fermions can be obtained by diagonalizing $\mathcal{H}_{total}$ in Eq. (1), which yields

$$E_k^{\pm} = \pm\sqrt{\left(v_F k\right)^2 + \left(J_{ex} M/2\right)^2} \quad , \tag{2}$$

where $k^2 \equiv k_x^2 + k_y^2$. Hence, an energy gap $\Delta = (J_{ex}M)$ opens up at the Dirac point for a finite $c$-axis magnetization $|M| > 0$ according to Eq. (2).

Experimental evidences for the occurrence of long-range ferromagnetism in the surface state of 3D-TIs have been manifested by the observation of surface gap opening in angle resolved photoemission spectroscopy (ARPES) [15-17] and the confirmation of quantized anomalous Hall effect (QAHE) [18,19] in magnetic 3D-TIs $(Bi_{1-x}Cr_x)_2Te_3$. However, the microscopic mechanism [20, 21] that mediates long-range ferromagnetism in the surface state remains unclear. A number of puzzling phenomena, such as a surface gap opening at a temperature $T_c^{2D}$ much higher than the onset of bulk magnetization $T_c^{3D}$ [15-17,21], the absence of gap formation by direct surface magnetic doping [22], and the lack of direct STS evidence for either magnetism-induced surface gaps or spectroscopic magnetic impurity resonances [20], all suggest that further investigation is needed.

We report in this work direct evidence for magnetism-induced surface-state energy gaps and magnetic impurity resonances in 3D-TIs by STS studies of bilayer structures of $Bi_2Se_3$ and Cr-doped $Bi_2Se_3$. The bilayer samples were grown by molecular beam epitaxy (MBE) on InP (111) single crystalline substrates, with an updoped $Bi_2Se_3$ layer of varying thicknesses, $d_1$ quintuple layers (QLs), on top of a Cr-doped $Bi_2Se_3$ layer of a fixed thickness $d_2$ = 6-QL. These bilayer structures ensured that magnetism may be observed in the undoped $Bi_2Se_3$ through the proximity effect for sufficiently small $d_1$ values, which prevented possible complications due to Cr-doping induced changes in the electronic bandstructures of $Bi_2Se_3$. Finally, we discuss the implications of our findings on applications of magnetically doped topological insulators to spintronics and quantum information technology.

## 2. Methods

The samples investigated in this work consisted of MBE-grown bilayer structures as schematically shown in figure 1(a), where $d_1$ = 1, 3, 5, 7-QL for the 10% Cr-doping level, and $d_1$ = 1-QL for 5% Cr-doping. Hereafter we use the nomenclature ($d_1$+$d_2$)-$x$% to denote our samples. Details of the growth process, structural characterizations and ARPES studies of these bilayer samples have been reported elsewhere [23-25]. Bulk electrical transport measurements on these samples revealed the appearance of anomalous Hall resistance at $T \le T_c^{3D} \sim 25$ K, as exemplified in figure 1(b).

For the STM studies, each bilayer sample was capped with ~ 1 nm Se inside the MBE growth chamber for passivation immediately after the bilayer growth. The sample was subsequently transferred from the growth chamber via a vacuum suitcase to another vacuum chamber, where the sample was annealed at 150 to 200 $^{o}$C for 90 minutes under vacuum (< $10^{-5}$ Torr) to remove the Se capping layer. The exposed bilayer sample was cooled to 300 K in vacuum, and then the sample-containing chamber was filled with Ar gas and loaded into an Ar-filled glove box, where the sample was removed from the chamber and transferred to the STM probe placed in the same glove box. The STM probe was sealed, transferred to its cryostat, and then evacuated down to ~ $10^{-10}$ Torr at liquid helium temperatures. The variable temperature range achievable for our homemade STM system was from 300 K to ~ 10 K, and a superconducting magnet was available to provide magnetic fields up to ~ 7 Tesla.

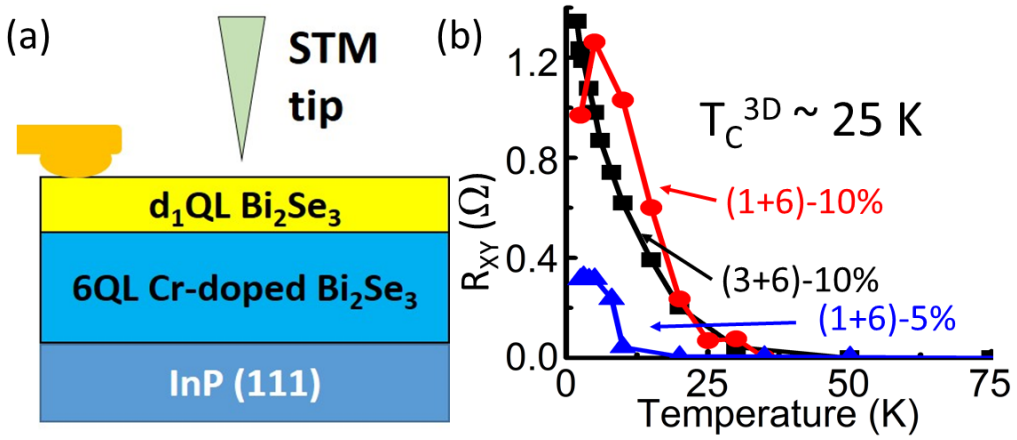


**Figure 1. (a)** Schematics of the side view of a $Bi_2Se_3$ bilayer sample, showing an undoped $Bi_2Se_3$ layer of a thickness $d_1$-QL on top of a Cr-doped $Bi_2Se_3$ layer of a thickness 6-QL grown on InP (111). A gold contact was placed on top of $d_1$. (b) Temperature dependent Hall resistance measurements on the $Bi_2Se_3$ bilayer samples at $H$ = 0, showing the onset of anomalous Hall effect below $T_c^{3D} \sim 25\,\mathrm{K}$.

## 3. Results and analysis

In this work both topographic and spectroscopic studies were made on all samples as a function of $T$ (from 300 K to 15 K) and $H$ (from 0 to 3.5 Tesla) using the variable temperature STM.

### *3.1. Structural characteristics from surface topographic studies*

The surface topography on large scales revealed pyramid-like terraces with steps corresponding to single atomic layers, as described previously [23]. For an averaged, nominal top layer thickness $d_1$-QL, the local thickness of the top layer could vary up to 1-QL. Atomically resolved topographic images exhibited triangular lattice patterns that were consistent with that of pure $Bi_2Se_3$, as exemplified in figure 2(a) and figure 2(b) for (1+6)-10% and (5+6)-10% samples, respectively. On the other hand, the Fourier transformation (FT) of the surface topography appeared to be dependent on $d_1$. We found that FT of the (1+6)-10% topography showed an expected hexagonal Bragg diffraction pattern for $Bi_2Se_3$ plus an additional, faint superlattice structure (figure 2(c)), which may be attributed to the underlying Cr-doped $Bi_2Se_3$. For instance, a periodic substitution of Cr for Bi as exemplified in figure 2(f) for a two-dimensional projection of the two Bi-layers within one-QL yields a FT pattern (figure 2(e)) similar to that in figure 2(c). This superlattice structure corresponds to a local Cr concentration of 1/12. Another similar structure with a local Cr concentration of 1/8 (figure 2(h)) is also feasible within experimental uncertainties of the superlattice constant and its angle relative to the Bi lattice (figure 2(g)). In contrast, the FT in figure 2(d) for the surface topography of a (5+6)-10% sample only revealed the hexagonal diffraction pattern of pure $Bi_2Se_3$ due to the relatively thick $d_1$ layer. Interestingly, we note that the FT topography of the (1+6)-5% samples also agreed with figure 2(d), suggesting random Cr substitutions of Bi for a smaller Cr concentration, which is consistent with the randomly distributed Cr clusters found with STM studies directly on 2% Cr-doped $Bi_2Se_3$ [26].

### *3.2. Zero-field spectroscopic studies*

For the zero-field studies, tunneling conductance ($dI/dV$) *vs*. biased voltage ($V = E/e$) measurements were carried out on each sample over multiple areas, followed by detailed analysis of the spatially

resolved spectral characteristics. While apparent spatial variations were found in all samples, systematic investigations led to several general findings. First, all samples revealed gapless Dirac tunneling spectra at 300 K. Second, with decreasing $T$ there were two distinctly different types of spectral characteristics: For samples with nominal $d_1$ = 5 and 7, the tunneling spectra remained gapless for all $T$, except for occasional areas where the actual $d_1$ values in the nominal $d_1$ = 5 sample were ~ 4. In contrast, for samples with nominal $d_1$ = 1 and 3, the majority spectra revealed gapped features at $T < T_c^{2D}$, and the temperature evolution for all samples are exemplified in figure 3 (a)-(d). Third, the surface gap $\Delta(\mathbf{r},T)$, obtained by the spectral analysis illustrated in figure 3(e), appeared to be spatially inhomogeneous where **r** denotes the two-dimensional spatial coordinate.

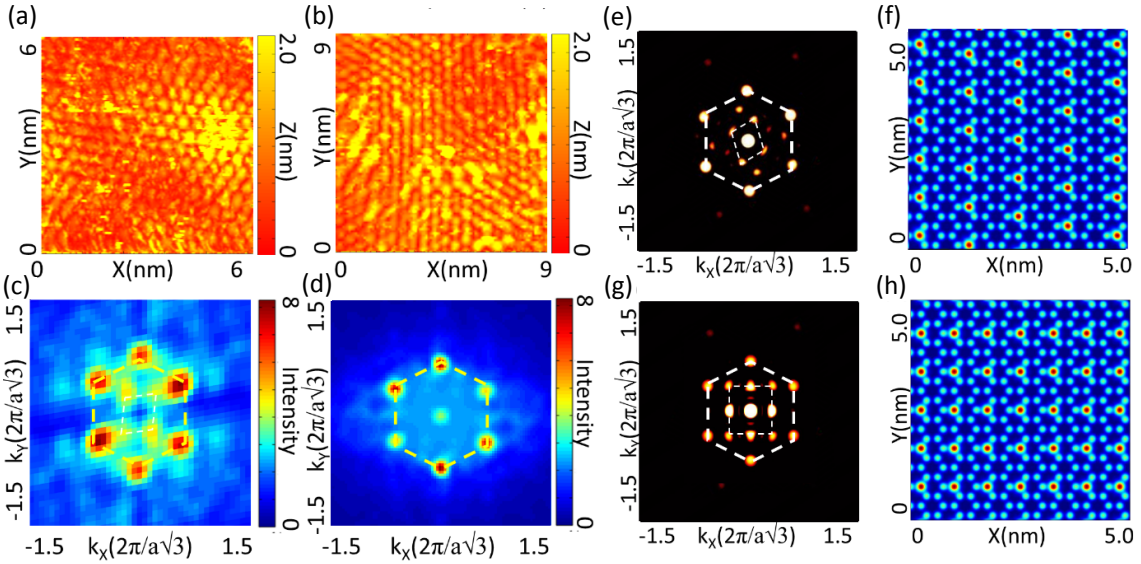


**Figure 2.** Structural characteristics of MBE-grown $Bi_2Se_3$ bilayer samples on InP (111): (a) Surface topography of a (1+6)-10% sample over an area of (6×6) nm$^2$, showing a triangular lattice structure. (b) Surface topography of a (5+6)-10% sample over an area of (6×6) nm$^2$, showing a triangular lattice. (c) Fourier transformation (FT) of the surface topography in a (1+6)-10% sample, revealing a dominant hexagonal reciprocal lattice structure and a secondary superlattice of a much weaker intensity, probably coming from the underlying Cr-doped $Bi_2Se_3$ layer. Here "a" in the reciprocal space scale ($2\pi/a\sqrt{3}$) refers to the in-plane nearest neighbor distance between Bi (Se) and Bi (Se). (d) FT of the surface topography on a (5+6)-10% sample, showing a purely hexagonal reciprocal lattice. (e) Simulated FT of the 1/12 Cr-substituted Bi layer illustrated in (f), showing a FT similar the data in (c). Here the blue dots represent Bi atoms and the red dots represent Cr substitutions. (g) Simulated FT of the 1/8 Cr-substituted Bi layer illustrated in (h), showing a FT also similar the data in (c) within experimental errors.

For a given **r**, $\Delta$ mostly increased with decreasing $T$ except near $T_x$ ~ (110±10) K where a slight dip appeared, and eventually saturated to a maximum value at $T \ll T_c^{2D}$, as exemplified by the $T$ evolution of the gap maps and the corresponding gap histograms in the left and middle panels of figure 4 (a)-(c) for the (1+6)-5%, (1+6)-10% and (3+6)-10% samples, and also summarized in the right panels for the temperature dependence of the corresponding mean gap $\overline{\Delta}(T)$. Here the mean gap value $\overline{\Delta}$ at a given $T$ was determined from the peak value of Gaussian fitting to the gap histogram, and the errors were determined from the one sigma linewidth of the Gaussian fitting. Based on the data for $\overline{\Delta}(T)$, the onset $T$ for the surface gap opening was found to be $T_c^{2D}$ = (240 ± 10) K for $x$ = 10% and $T_c^{2D}$ = (210 ± 10) K for $x$ = 5%, significantly higher than the bulk Curie temperature $T_c^{3D}$ ~

25 K obtained from the onset temperature of the anomalous Hall effect. We note that our finding of $T_c^{2D} \gg T_c^{3D}$ is consistent with previous reports on other families of 3D-TIs [15-17].

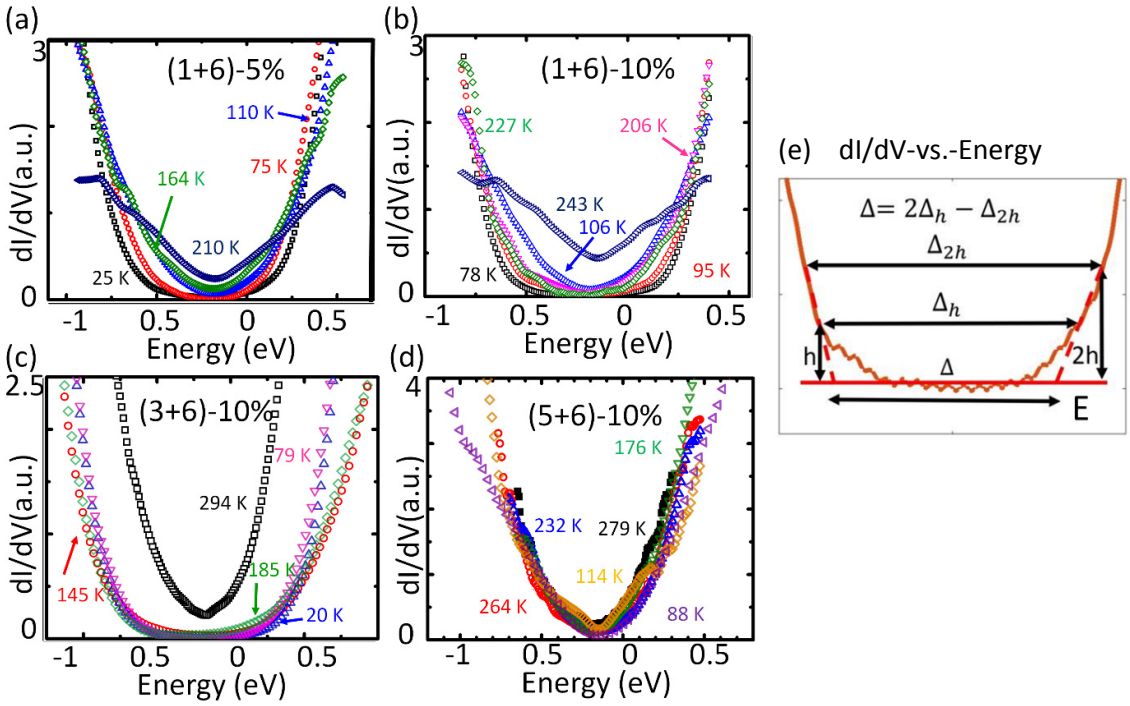


**Figure 3.** Temperature evolution of representative normalized tunneling conductance spectra of ($d_1$ +$d_2$)-$x$% bilayer samples taken at $H$ = 0: (a) (1+6)-5%, (b) (1+6)-10%; (c) (3+6)-10%, and (d) (5+6)-10%. For samples with $d_1$ = 1 and 3, each representative spectrum in (a)-(c) at a given $T$ was determined by first taking the spatially resolved tunneling spectra over a fixed area of the sample, plotting the histogram of the gap values to determine the mean gap $\overline{\Delta}$ over this area, and then averaging those spectra with gap values within one sigma of $\overline{\Delta}$. To compensate for the thermal drift of the STM tip and to ensure that the spectral analysis was carried out over the same sample area for all different temperatures, we compared the topographic images taken at all temperatures to identify the overlapped areas. With this procedure, finite gaps were consistently found to develop at low temperatures for samples with $d_1$ = 1 and 3 as exemplified in (a)-(c), whereas all spectra were gapless for samples with $d_1$ = 5 and 7, as exemplified in (d). (e) Schematic illustration showing how the gap is estimated from a realistic normalized tunneling conductance spectrum: Defining the conductance of the inflection point in the tunneling spectrum as $h$ and the corresponding energy difference between the spectral inception points as $\Delta_h$, we identify $\Delta_{2h}$ for the tunneling conductance at $2h$, and then extrapolate an effective gap $\Delta$ at zero conductance from the formula $\Delta = 2\Delta_h - \Delta_{2h}$. The maximum gap thus obtained is consistent with the theoretical values (0.3 ~ 0.5 eV) from the densities of states of $Se^{I,II}$ in Cr-doped $Bi_2Se_3$ [26].

The inhomogeneous gap distribution may be the result of multiple reasons. First, the Cr-substitution of Bi may not be uniform as the result of the size mismatch that could induce significant lattice strain and inhomogeneous ferromagnetism. Second, the magnetic moments of individual Cr may not be perfectly aligned along the sample c-axis in the absence of an external magnetic field. Given that only $c$-axis magnetization component can induce an energy gap in the surface state of 3D-TIs according to Eqs. (1) and (2), varying spin alignments in different magnetic domains would result in varying surface gaps [27]. Third, the sample surface exhibited terrace-like structures with thickness variations up to 1-QL [23], which could give rise to different proximity-induced gaps.

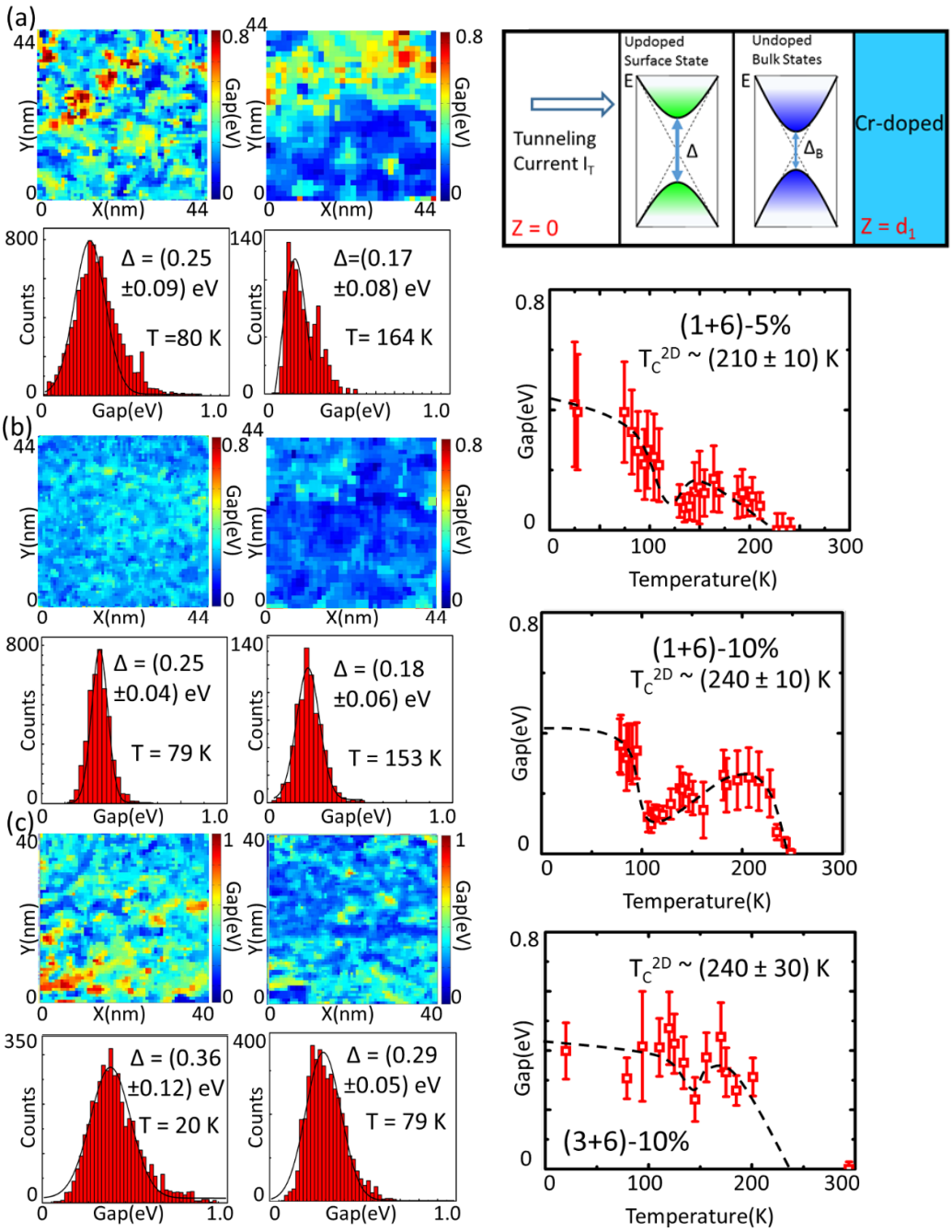


**Figure 4.** Temperature evolution and spatial distribution of the surface gap at $H = 0$: (a) Gap maps and the corresponding gap histograms of a (1+6)-5% sample taken at $T = 80$ K (left panels) and $T = 164$ K (middle panels), and the temperature dependence of the mean gap $\overline{\Delta}$ (second right panel). (b) Gap map and the corresponding gap histograms of a (1+6)-10% sample taken at $T = 79$ K (left panels) and $T = 153$ K (middle panels), and the temperature dependence of the mean gap $\overline{\Delta}$ (third right panel). (c) Gap maps and the corresponding gap histograms of a (3+6)-10% sample taken at $T = 20$ K (left panels) and $T = 79$ K (middle panels), and the temperature dependence of the mean gap $\overline{\Delta}$ (fourth right panel). The first right panel is a schematic illustration of the spatially varying electronic structure experienced by the tunneling current, showing the dominance of the surface state gap $\Delta$ over the bulk gap $\Delta_B$ in determining the measured spectral gap in STS.

*3.3. Finite-field spectroscopic studies*

We further investigated the effect of increasing *c*-axis magnetic field (*H*) on the gap distribution over the same area of each sample at a constant *T*. As exemplified in figure 5(a)-(f) for samples of (1+6)-5% and (3+6)-10% taken at $T = 18$ K and $H = 0$, 1.5 T and 3.5 T, the gap maps became increasingly homogeneous and the mean gap value $\bar{\Delta}$ derived from the histogram also increased slightly with increasing *H*. This finding suggests that the observed surface gap is consistent with *c*-axis ferromagnetism induced by Cr-doping and proximity effect, and the characteristic field for saturating the surface state ferromagnetism appears to be larger than that for saturating the bulk ferromagnetism [24], probably due to the helical spin textures of the former. The small but finite residual gap inhomogeneity in high fields may be attributed to spatially inhomogeneous Cr-distributions and the $d_1$ variations.

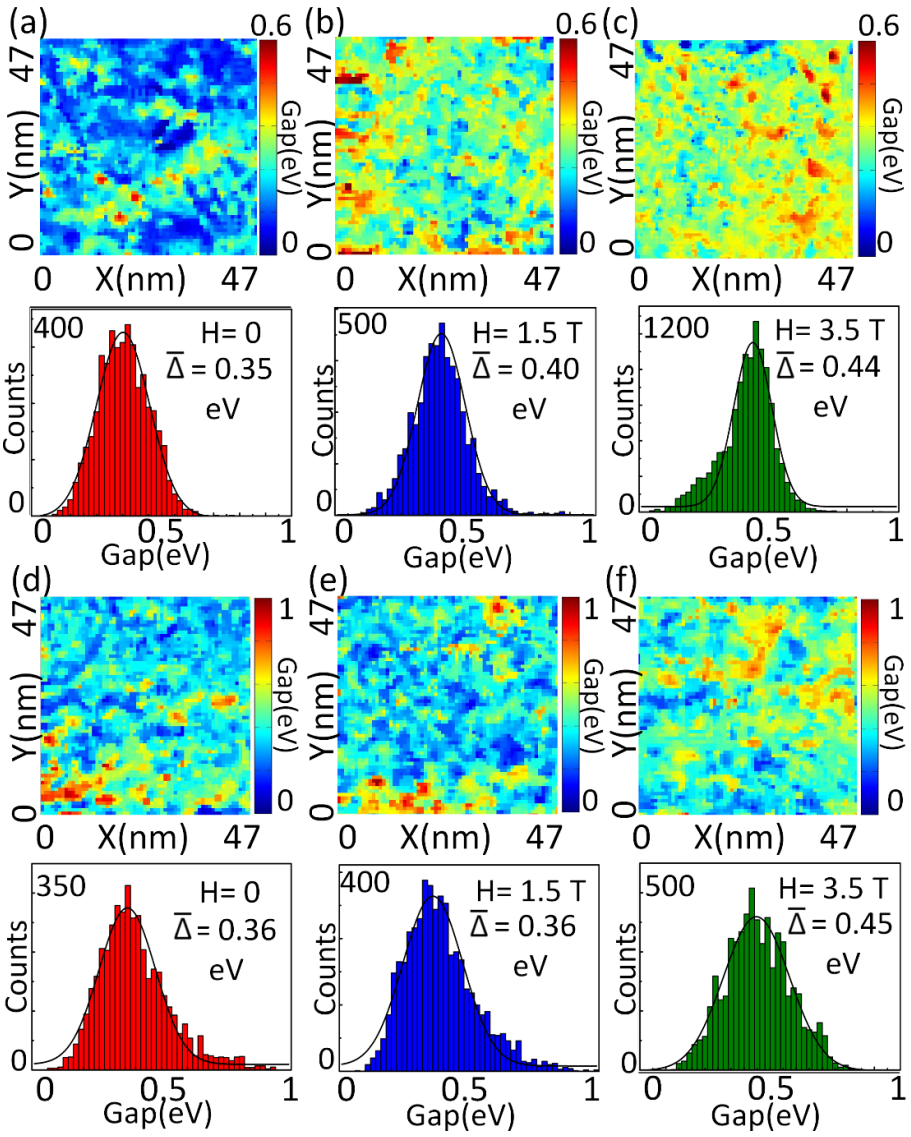


**Figure 5.** Evolution of the surface gap distribution at $T = 18$ K with applied c-axis magnetic field: (a-c) Gap maps (upper panels) and the corresponding gap histograms (lower panels) of a (1+6)-5% sample taken at $H = 0$, 1.5 T and 3.5 T over the same (20 × 20) nm$^2$ area. (d-f) Gap maps (upper panels) and the corresponding gap histograms (lower panels) of a (3+6)-10% sample taken at $H = 0$, 1.5 T and 3.5 T over the same (20 × 20) nm$^2$ area.

*3.4. Minority spectra*

While the majority of the tunneling spectra in the (1+6)-5%, (1+6)-10% and (3+6)-10% samples revealed gapped characteristics for $T < T_C^{2D}$, spatially localized and intense conductance peaks were occasionally observed along the borders of gapless and gapped regions, as exemplified in figure 6 (a)-(d) for a (1+6)-5% sample and in figure 6 (f) for a (1+6)-10% sample. These long-lived minority spectra either consisted of a single sharp conductance peak at a small negative energy $E = E_-$ near the Dirac point $E_D$; or comprised of double conductance peaks (figure 6(b)) at $E = E_-$ and $E = E_+$, where $E_+$ is near the Fermi energy $E_F = 0$. These double-peak spectral characteristics were consistent with theoretical predictions for magnetic impurity resonances [20]. Further, the numbers of both single- and double-peak impurity resonances at $H = 0$ were found to increase rapidly near $T_C^{2D}$ (figure 6(f)). In contrast, all resonances disappeared under a large c-axis magnetic field at low $T$ when gapless regions diminished.

We attribute the sharp impurity resonances to isolated Cr-impurities that diffused from the $d_2$ layer into the $d_1$ layer because they were only found in zero-field along the borders between gapless and gapped regions, and then disappeared under a large $c$-axis magnetic field when gapless regions diminished. The temperature dependence at $H = 0$ as exemplified in figure 6 (f) may be understood as the result of weakening ferromagnetism near $T_C^{2D}$, so that more Cr-impurities became decoupled and acted like isolated impurities. The strong spatial localization and long lifetime of these magnetic impurity resonances at $H = 0$ may be attributed to topological protection of the surface state in 3D-TIs when the Dirac energy $E_D$ is relatively close to $E_F$, similar to the case for non-magnetic impurities [20, 28]. Our finding of atomically sharp impurity resonances due to diffused Cr atoms into the undoped $d_1$ layer differs from direct STS studies of 2% Cr-doped $Bi_2Se_3$ [26], where Cr substituted Bi in clusters and so did not behave like atomically isolated magnetic impurities in the surface state of pure $Bi_2Se_3$.

## 4. Discussion

The dependence of the spectral characteristics on $T$, $H$, $x$ and $d_1$ for the bilayer samples are all consistent with the scenario that the appearance of a surface-state gap was induced by the proximity effect of predominantly $c$-axis ferromagnetism in the Cr-doped bottom layer. The appearance (absence) of gapped tunneling spectra below $T_C^{2D}$ for bilayer samples with $d_1 \leq$ 3-QL ($d_1 \geq$ 5-QL) suggests that the proximity effect due to $c$-axis magnetic correlation is limited to ~ 4-QL.

Concerning the physical feasibility of a relatively high $T_C^{2D}$, we note that the energy splitting of the double-peak spectrum associated with isolated magnetic impurities in the surface state is comparable to the ferromagnetic exchange coupling $J_{ex}$ [20]. Noting that the mean-field Curie temperature may be estimated from $J_{ex}$ via the relation $k_B T_C^{2D} \sim S(S+1)(J_{ex}/3)$ [29] and that $J_{ex} \sim$ 0.1 eV, we obtain $T_C^{2D} \sim$ 250 K by assuming $S = 1/2$. While this rough estimate does not include the screening effect from Dirac fermions, it is still comparable to our STS measurements of $T_C^{2D} \sim$ 240 K for $x = 10\%$ and $T_C^{2D} \sim$ 210 K for $x = 5\%$ for the observed surface ferromagnetism, and is much higher than the bulk $T_C^{3D} \sim$ 25 K. The disparity of $T_C^{2D}$ and $T_C^{3D}$ may be attributed to the different microscopic mechanisms for mediating ferromagnetism between the surface state of a helical metal and the bulk state of an insulator. Additionally, the non-monotonic $T$-dependence of the tunneling gap for all samples with $d_1 = 1$ and 3 (figure 3) may be indicative a crossover from 2D to 3D ferromagnetism. While the microscopic mechanism responsible for $T_C^{2D} \gg T_C^{3D}$ requires further investigation, the relatively high $T_C^{2D}$ values are promising for realistic spintronic applications, particularly if our findings may be generalized to more homogeneously Cr-doped 3D-TIs such as $(Bi_{1-x}Cr_x)_2Te_3$ [24].

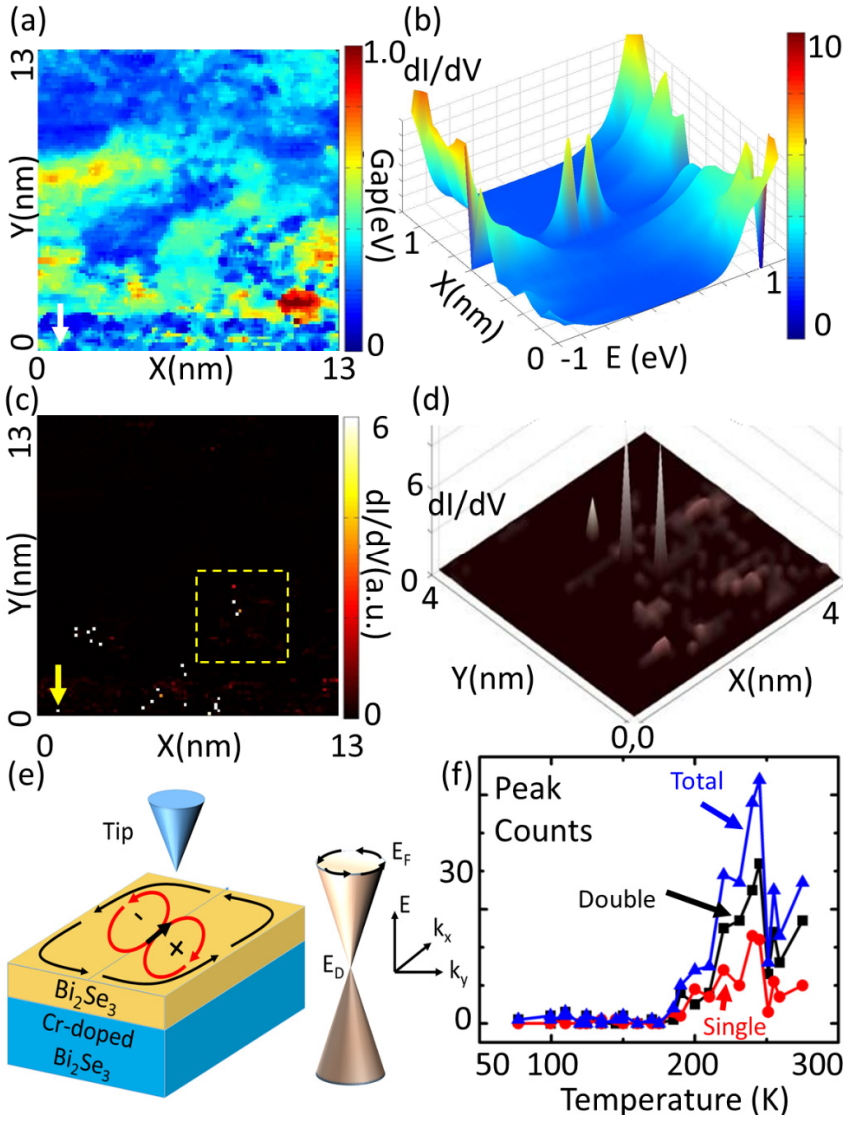


**Figure 6.** Spectral characteristics of isolated magnetic impurities: (a) Gap map of a (1+6)-5% bilayer sample taken at 80 K over an area of (13×13) nm$^2$, showing both spatially inhomogeneous gaps and some gapless regions (dark blue). The arrow indicates a site where a spatially localized double-resonant spectrum in (b) is observed. (b) Sharp resonances of an isolated impurity are manifested in the ($dI/dV$) vs. $E$ and $X$ plot, where $X$ is a horizontal linecut across an isolated impurity indicated by the arrow in (c). The sharp double resonant peaks appear at $E = E_-$ and $E = E_+$, where $E_-$ is near $E_D$ and $E_+$ is near $E_F$. (c) Tunneling conductance map taken at $E = E_-$ over the same area as in (a), showing spatially isolated conductance peaks in bright sharp spots. (d) Two-dimensional distribution of the tunneling conductance at bias voltage $V = (E_-/e)$ over a (4×4) nm$^2$ area indicated by the dashed box in (c), showing three sites with intense impurity resonances. (e) Schematics of a topological defect (red arrows of opposite helicity) due to an isolated magnetic impurity in the surface-state Dirac spin textures (counterclockwise black arrows). (f) $T$-evolution of the counts of single- and double-peak and total impurity resonances over a (20×20) nm$^2$ area of a (1 + 6)-10% sample, showing a rapid increase in the number of impurity resonances near $T_c^{2D}$ for both the single- and double-peak resonances.

We also remark that the undoped $Bi_2Se_3$ layer in our bilayer samples should *not* be considered as an isolated thin film on a "substrate" of Cr-doped $Bi_2Se_3$ because of the seamless growth of the undoped $Bi_2Se_3$ top layer on the isostructure Cr-doped $Bi_2Se_3$ bottom layer [24], leading to an effective total thickness of $(d_1 + d_2)$-QL. In contrast, for ultra-thin TI films on dissimilar substrates, an energy gap would open up due to the coupling between the top and bottom topological surface states, and a Rashba-like coupling with further energy splitting in momentum would be expected due to the asymmetric chemical potentials between the surface of the thin film and its interface with a dissimilar substrate [30]. This Rashba-like coupling has indeed been confirmed by ARPES [31] and STS [32] studies for 2-QL to 5-QL $Bi_2Se_3$.

Another seemingly puzzling point worth commenting on is that our empirical estimates of the proximity-induced surface gap in $Bi_2Se_3$ appeared to be comparable or even slightly larger than the bulk gap of $Bi_2Se_3$. One may question whether it is feasible for a magnetism-induced surface gap of a topological insulator to exceed its bulk gap. Here we emphasize that our bilayer structures ensured that Cr-doping in the bottom $Bi_2Se_3$ layer induced long-range magnetization to the top $Bi_2Se_3$ layer through proximity effect without altering the electronic bandstructures of the latter. Hence, the Hamiltonian in Eq. (1) is fully justified for the surface state of the top $Bi_2Se_3$ layer in our bilayer samples, and the resulting surface gap $\Delta = (J_{ex}M)$ is simply a function of the ferromagnetic exchange coupling $J_{ex}$ and the magnitude of magnetization $M$ without any other constraints. We further note that the gap value determined from STS studies would be dominated by the local gap of the surface layer, whereas the gap value determined from ARPES would be largely dominated by the smallest gap value over an extended surface area. In this context, the surface gap of an inhomogeneous sample would tend to be larger if determined from STS than if determined from ARPES.

The appearance of both single- and double-peak magnetic impurity resonances is suggestive of two types of topological defects associated with an isolated magnetic impurity: The single-peak resonance may be attributed to a helical Dirac spin texture coupling to a magnetic moment pointing along the *c*-axis, whereas the double-peak resonance is associated with two opposite chiral spin textures of Dirac fermions coupling to an in-plane magnetic moment [20], as illustrated in figure 6 (e). Our assignment of the single-peak resonances in this work to the helical Dirac spin texture coupled with isolated *c*-axis magnetic moments can be justified by their strong and non-monotonic temperature dependence near $T_C^{2D}$ (figure 6 (f)), and also by their suppression under large *c*-axis magnetic fields. In contrast, our previous studies of non-magnetic impurity resonances in pure $Bi_2Se_3$ MBE-grown thin films [28] did not find any dependence of their occurrences on either the temperature or the applied magnetic field, implying that the physical origin of the single-peak resonances in pure $Bi_2Se_3$ is fundamentally different from that of the single-peak resonances observed in the bilayer systems.

Our finding of occurrences of impurity resonances only along the borders of gapped and gapless regions is consistent with suppressed long-range magnetic order along the boundaries between the *c*-axis oriented (gapped) and in-plane oriented (gapless) magnetic domains [27]. Thus, proximity-induced magnetization in the top $Bi_2Se_3$ layer is also much suppressed for regions above the boundaries of *c*-axis and in-plane magnetic domains [27], and Cr-ions diffused into these regions were more likely to decouple from long-range magnetization and became effectively isolated magnetic impurities, particularly with the assistance of thermal fluctuations at sufficiently high temperatures (figure 6 (f)).

Finally, we note that the spin textures associated with an in-plane magnetic impurity may be considered as a stable "topological bit" with two levels associated with the two opposite spin chirality. In principle, for a completely isolated topological bit, the mixing of the two-level states may be tuned by a local *c*-axis magnetic field. Further, for $E_F \rightarrow E_D$ these topological bits are long-lived as the result of topological protection. On the other hand, tuning $E_F$ away from $E_D$ will result in increasing coupling among spatially separated topological bits [20], which may be viewed as inducing an effective entanglement of wave functions among these topological bits. The feasibility of tuning the

mixing of the two levels within a topological bit by an external magnetic field and the coupling among spatially separated bits by gating the Fermi level may present an interesting opportunity for applications these topological bits to quantum information technology.

## 5. Conclusion

We have demonstrated scanning tunneling spectroscopic evidences for magnetism-induced massive Dirac spectra and topological defects in the surface state of MBE-grown 3D-TIs that consisted of bilayers of undoped $Bi_2Se_3$ on top of Cr-doped $Bi_2Se_3$. For an undoped layer thinner than or equal to 3-QL, proximity-induced ferromagnetism was manifested by the appearance of a surface gap $\Delta$ below a transition temperature $T_c^{2D} > 200$ K, and the value of $T_c^{2D}$ was found to be Cr-doping ($x$) dependent and also much higher than the bulk ferromagnetic transition temperature $T_c^{3D}$ (~ 25 K). The gap distribution was spatially inhomogeneous, and its average value and spatial homogeneity at low $T$ increased with $H$ and $x$, confirming its magnetic origin. Topological defects associated with helical spin textures of the Dirac fermions around isolated magnetic impurities were also manifested as long-lived sharp double-peak spectral resonances along the borders of gapped and gapless regions. The strong localization and long life-time of these magnetic impurity resonances represent interesting topological bits that are potentially useful for applications to quantum information.


## Acknowledgement

This work at Caltech was jointly supported by DARPA and NSF. The work at UCLA was supported by DARPA. We thank Professors Gabriel Aeppli, Alexei Kitaev, Nai-Phaun Ong and Thomas Rosenbaum for useful discussions.


## References


[1] Wen X-G 1995 *Adv. Phys.* **44** 405
[2] Qi X L and Zhang S-C 2011 *Rev. Modern Phys.* **83** 1057
[3] Hasan M Z and Kane C L 2010 *Rev. Modern Phys.* **82** 3045
[4] Kane C L and Mele E J 2005 *Phys. Rev. Lett.* **95** 146802
[5] Kane C L and Mele E J 2005 *Phys. Rev. Lett.* **95** 226801
[6] Bernevig B A and Zhang S-C 2006 *Phys.Rev. Lett.* **96** 106802
[7] Fu L and Kane C L 2007 *Phys. Rev. B* **76** 045302
[8] Qi X L, Hughes T L and Zhang S-C 2008 *Phys. Rev. B* **78** 195424
[9] Fu L and Kane C L 2008 *Phys. Rev. Lett.* **100** 096407
[10] Fu L and Kane C L 2009 *Phys. Rev. B* **79** 161408(R)
[11] Qi X-L, Li R, Zhang J and Zhang S-C 2009 *Science* **323** 1184
[12] Nomura K and Nagaosa N 2011 *Phys. Rev. Lett.* **106** 166802
[13] Qi X-L, Wu Y S and Zhang S-C 2006 *Phys. Rev. B* **74** 085308
[14] Alicea J 2012 *Rep. Prog. Phys.* **75** 076501
[15] Chen Y L *et al.* 2010 *Science* **329** 659
[16] Wray L A *et al.* 2011 *Nat. Phys.* **7** 32
[17] Xu S Y *et al.* 2012 *Nat. Phys.* **8** 616
[18] Yu R W *et al.* 2010 *Science* **329** 61
[19] Chang C-Z *et al.* 2013 *Science* **340** 167
[20] Biswas R R and Balatsky A V 2010 *Phys. Rev. B* **81** 233405
[21] Rosenberg G and Franz M 2012 *Phys. Rev. B* **85** 195119
[22] Scholz M R *et al.* 2012 *Phys. Rev. Lett.* **108** 256810
[23] He L *et al.* 2013 *Phys. Status Solidi RRL* **7** 50
[24] Kou X *et al.* 2013 *Nano Lett.* **13** 4587
[25] Lang M *et al.* 2012 *Nano Lett.* **13** 48
[26] Chang C-Z *et al.* 2014 *Phys. Rev. Lett.* **112** 056801

[27] Lang M *et al.* 2014 *Nano Lett.* **14** 3459
[28] Teague M-L *et al.*, 2012 *Solid State Comm.* **152** 747
[29] Kittel C *Introduction to Solid State Physics*
[30] Shan W Y, Lu H-Z and Shen S-Q, 2010 *New J. Phys.* **12**, 043048
[31] Zhang Y *et al.* 2010 *Nat. Phys.* **6** 58
[32] Yeh N-C *et al.* 2012 *EPJ Web of Conferences* **23** 00021